Microearthquake patterns following the 1998 eruption of Axial Volcano, Juan de Fuca Ridge: Mechanical relaxation and thermal strain

Robert A. Sohn
Woods Hole Oceanographic Institution, Woods Hole, Massachusetts, USA

Andrew H. Barclay
University of Washington, School of Oceanography, Seattle, Washington, USA

Spahr C. Webb
Lamont Doherty Earth Observatory, Palisades, New York, USA

Received 18 March 2003; revised 1 October 2003; accepted 15 October 2003; published 14 January 2004.

[1] Ocean bottom seismic networks deployed following the 1998 eruption of Axial seamount reveal an evolving pattern of microearthquake activity associated with subsurface magmatism and thermal strain. Seismicity rates decay steadily over 15 months of observation (February 8, 1998, to April 30, 1999), consistent with a trend toward thermal and mechanical equilibrium in the shallow crust after the magmatic event. Immediately after the eruption, seismicity rates were high for about 60 days in the southeast corner of the caldera where lava flows from the 1998 eruption were mapped. A small burst of seismic activity was observed on the southeast shoulder of the volcano from 100 to 150 days after the eruption. These events, which are characterized by slip on nearly vertical faults in the shallow crust, extend about 6 km from the southeast corner of the caldera and overlie a mid-crustal low-velocity zone. After this episode, seismicity rates remain low until the end of the observation period, 455 days after the eruption. Shallow ($\sim$0.7 km depth) events, consistent with thermal contraction and volume changes of $\sim 2 \times 10^{-3}$ m^3 in $\sim$5 m^3 sources, are observed in individual clusters beneath hydrothermal vents within the 1998 lava flow at the southeast edge of the caldera. Microearthquakes observed during the last 70 days of observation are distributed around the central caldera, most likely representing small amounts of subsidence on caldera faults during the final stages of equilibration following melt withdrawal associated with the 1998 eruption. *INDEX TERMS:* 3035 Marine Geology and Geophysics: Mid-ocean ridge processes; 7280 Seismology: Volcano seismology (8419); 8135 Tectonophysics: Hydrothermal systems (8424); *KEYWORDS:* microearthquakes, hydrothermal, magmatism

Citation: Sohn, R. A., A. H. Barclay, and S. C. Webb (2004), Microearthquake patterns following the 1998 eruption of Axial Volcano, Juan de Fuca Ridge: Mechanical relaxation and thermal strain, *J. Geophys. Res.*, *109*, B01101, doi:10.1029/2003JB002499.

1. Introduction

[2] Axial seamount is an underwater volcano located $\sim$460 km off the coast of the northwestern United States (Figure 1). Magmatism at Axial is fueled by mantle melting associated with the Cobb hot spot [*Desonie and Duncan*, 1990], a melting anomaly that has remained fixed in the hot spot reference frame for at least 26 Myr [*Dalrymple et al.*, 1987]. The volcano is the youngest feature in the Cobb-Eickelberg seamount chain, which intersects the northwest migrating (30 km/My) Juan de Fuca Ridge (JdFR) at Axial volcano, with the Coaxial segment to the north, and the Vance segment to the south (Figure 2).

0148-0227/04/2003JB002499$09.00

[3] The volcano has been extensively studied for more than 3 decades (for example, see the Special Section of *Journal of Geophysical Research*, volume *95*, issue B8), and has been continuously monitored for seismic activity by real-time hydroacoustic networks since 1993 [*Fox et al.*, 1994]. The volcano experienced a major magmatic event beginning on January 25, 1998, which was well-documented by a combination of hydroacoustic monitoring [*Dziak and Fox*, 1999a], *in situ* seafloor geodetic instrumentation [*Fox*, 1999; *Chadwick et al.*, 1999], and rapid response surveys (see the Special Section of *Geophysical Research Letters*, volume *26*, issue 23). Seismic activity (including broadband volcanic tremor) was focused on the volcano's summit for several hours, and then began migrating down the volcano's South Rift Zone (SRZ) at a rate of $\sim$0.23 m/s, reaching a maximum downrift distance

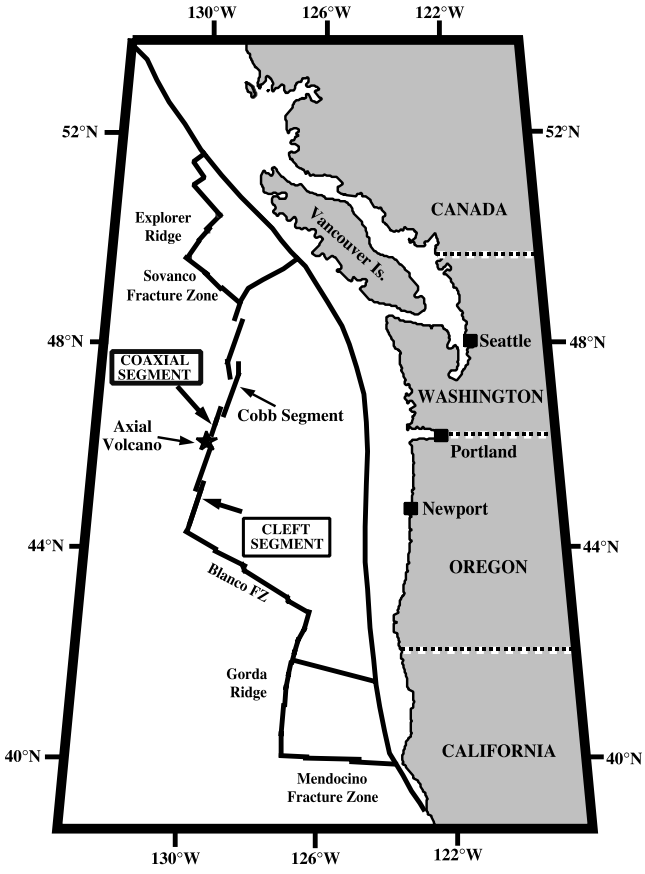

Figure 1. Area map of the Juan de Fuca Ridge (JdFR) with black star marking the position of our field area (Axial volcano).

of ~50 km in 2+ days. The seismic swarm on the volcano's summit lasted about 5 days, and continued at the distal end downrift for an additional 3–4 days.

[4] On the basis of observations with the DSRV *ALVIN*, the Canadian ROV *ROPOS*, and bathymetric difference mapping, it was determined that a 5.5-km-long by 0.7-km-wide sheet flow was erupted along the upper SRZ in the southeast corner of the central caldera (Figure 3) [*Embley et al.*, 1999; R. W. Embley and W. W. Chadwick, unpublished data, 2003]. Bathymetric difference mapping delineated the position of a second fresh lava flow on the SRZ at 45°52.5′N, which was subsequently confirmed by *ROPOS* observations to be fresh lobate and pillow lavas. The most recent estimate of total extrusive volumes associated with the 1998 eruption is $15–22 \times 10^6$ m^3 (W. W. Chadwick, personal communication, 2003), and total intrusive magma volumes (dikes) are estimated at $100–150 \times 10^6$ m^3.

[5] Records from bottom pressure recorders (BPRs) situated in the caldera during the eruption demonstrate that the depth of the caldera floor increased by 3.2 m and 1.4 m in the center and southeast edge of the caldera, respectively [*Fox et al.*, 2001]. Three of the seismic events on the summit were large enough to be detected by land seismic stations in the Pacific Northwest (M_w 4.8, 4.9, 4.8), and focal plane solutions indicate high angle (76–81°) normal faulting striking 348°NE–354°NE [*Dziak and Fox*, 1999a]. Acoustic extensometer data from the volcano's North Rift Zone (NRZ) exhibit an abrupt 4 cm contraction during the same time period, and these data, taken together, are consistent with bowl-shaped subsidence of the caldera and the withdrawal of 207×10^6 m^3 of magma from a point source at ~3.8 km depth [*Chadwick et al.*, 1999].

[6] In order to obtain a detailed understanding of microearthquake activity associated with the magmatic event we deployed an ocean bottom hydrophone (OBH) network on the volcano within 2 weeks of the eruption [*Sohn et al.*, 1999a]. We returned several times over the next year and a half to retrieve data and deploy additional seismic stations, and as a result we have acquired 455 days of continuous, local seismic data from Axial volcano. We observe systematic changes in the nature of seismic activity following the volcanic event, and we find that microearthquake activity is spatially correlated with the position of subsurface magma reservoirs and intrusions associated with the 1998 eruption. We attribute the microearthquakes to stress perturbations associated with the cooling of intruded magmas and adjustment of the caldera region to thermal and mechanical changes following the eruption. We examine the relationship between thermal strain in deep-sea hydrothermal systems and microearthquake activity in detail, and develop relationships between seismic moment and characteristic source volume for thermal cracking.

[7] Initial results from the first OBH deployment immediately after the eruption were previously reported by *Sohn et al.* [1999a]. In this paper we provide improved hypocenter estimates for those microearthquakes based on 3-dimensional seismic velocity models for Axial volcano derived from a recent refraction survey [*West et al.*, 2001; *Menke et al.*, 2002]. We also re-interpret the cause of some of the events based on the discovery of a previously unknown crustal low-velocity zone on the volcano's southeast shoulder [*West*, 2001; *Carbotte et al.*, 2002].

2. Experiment and Observations

[8] We deployed three seismic networks on and around Axial volcano following the 1998 magmatic event (Figure 2). The first network (SAX-OBH), consisting of seven OBH deployed on the volcano's central caldera and SRZ, returned continuous data from February 8 to July 28, 1998. A second seismic network (MAX-OBH), consisting of four OBH in a small aperture configuration in the southeast corner of the central caldera, was deployed upon recovery of the first and returned continuous data from August 4, 1998, to February 14, 1999. A third network (MAX-OBS), consisting of ten 4-component (hydrophone + three-axis geophone) ocean bottom seismometers (OBS), was deployed on the volcano, its proximal rift zones, and the adjoining mid-ocean ridge segments to the north and south. This network returned continuous data from January 23 to April 30, 1999, and was also used to record signals from a seismic refraction experiment [*Menke et al.*, 2002; *West et al.*, 2001]. Taken together, these networks provide 455 days of continuous seismic coverage at Axial volcano from February 8, 1998 to April 30, 1999, with the exception of a 6-day gap between July 29 and August 3, 1998. All of the data were digitized at 128 samples per second, with anti-aliasing filters set at 40 Hz.

[9] The seismic networks recorded signals from local, regional, and teleseismic events, along with periods of

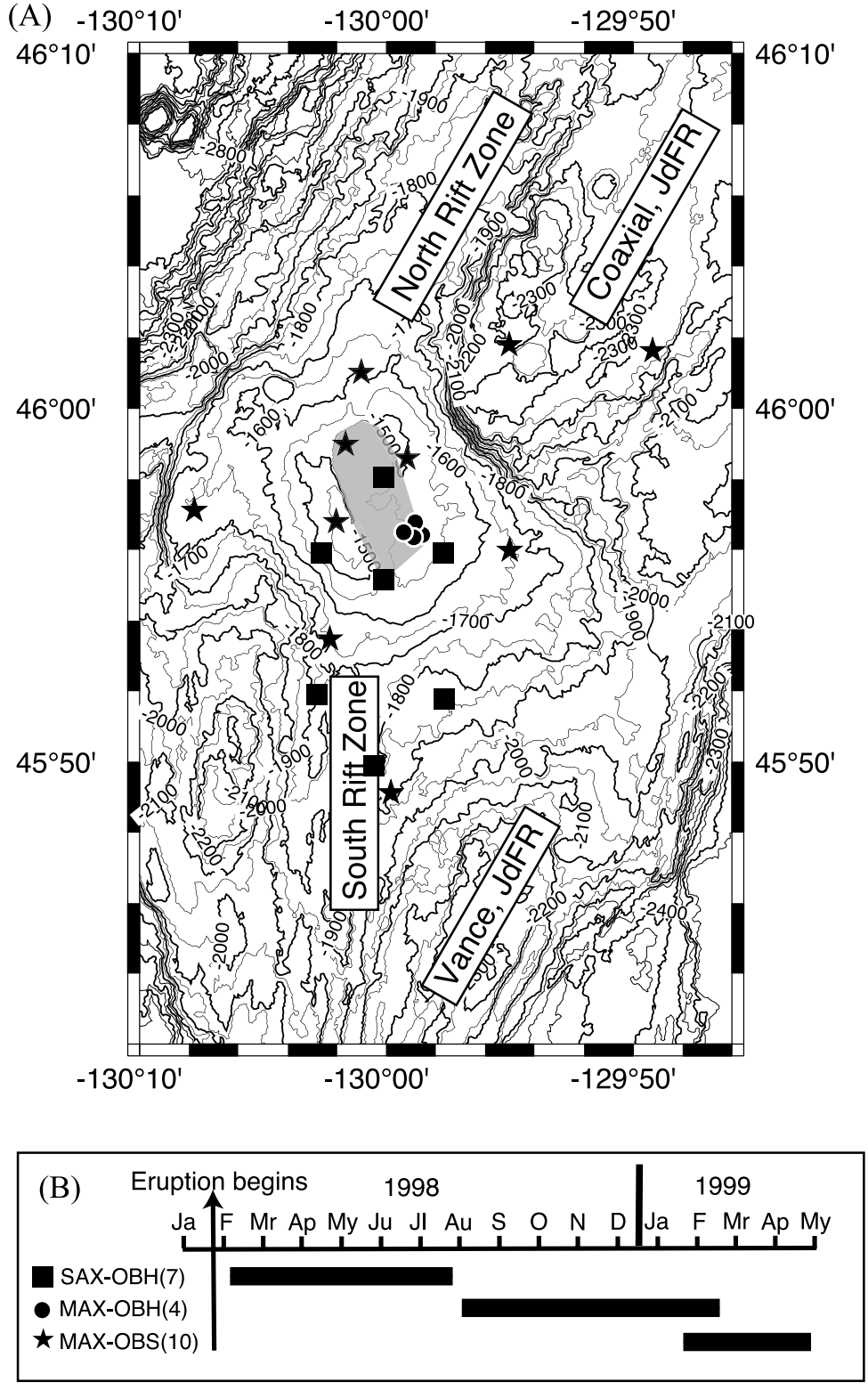

Figure 2. (a) Field area overview with seismic monitoring networks. Central caldera shaded gray. (b) Legend and time intervals for the seismic networks.

ubiquitous blue and fin whale calling. In this paper we focus solely on the local microearthquakes, which are characterized by impulsive body waves with durations of 1–3 s (Figures 4 and 5). Direct compressional (*P*) and sea-surface reflected compressional (*PwP*) arrivals are observed for essentially all events, though the amplitude and character of these arrivals can vary considerably from one event to the next and from station to station. Direct shear (*S*) arrivals are observed in all of the geophone (Figure 5), and some of the hydrophone records, but we only use *S* arrivals from geo-

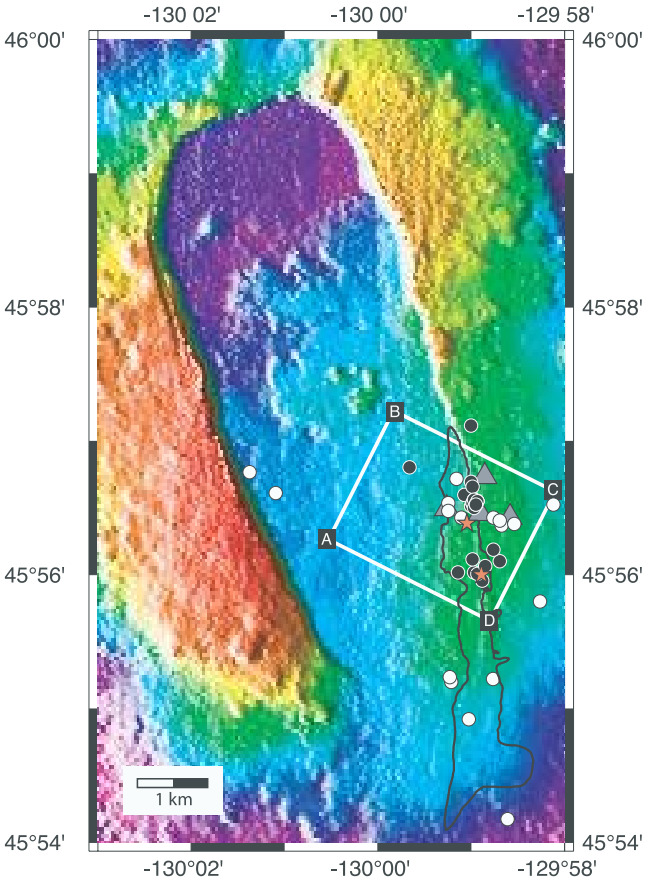

Figure 3. Detail of microearthquake activity in southeast corner of caldera (EM300 digital bathymetry courtesy of R. W. Embley and W. W. Chadwick). Only events with x-y errors <0.5 km are shown. White circles are events from SAX-OBH network and black circles are events from MAX-OBH network. Gray triangles are MAX-OBH station locations. Red stars are hydrothermal vent fields. Surface extent of 1998 lava flow (R. W. Embley and W. W. Chadwick, unpublished data, 2003) is delineated with a black line. Box ABCD is map view of volume cube in Figure 9.

phones in this analysis because we do not consider *S* arrival times determined from hydrophone records to be reliable.

3. Methods and Results

3.1. Hypocenter Parameters

[10] An event detection algorithm was applied to the raw data records to find local microearthquakes detected by three or more stations. We first identified time intervals on the hydrophone channel of each instrument for which the energy averaged over a 1-s period window exceeded the energy averaged over a 10-s window by a factor of 2. These parameters were chosen to maximize the number of triggers on potentially pickable earthquake arrivals while minimizing triggers on data spikes and other spurious signals. For instruments with poor quality hydrophone data, we used the vertical geophone channel. Events that triggered in this way on three or more instruments within a 10-s period were manually inspected in order to identify local earthquakes. *P*, *S*, and *PwP* phases, and their uncertainties, were hand picked for each event when possible.

[11] Hypocentral estimates were made using a grid-search algorithm. Theoretical *P* and *PwP* travel time grids (dx = dy = 0.5 km, dz = 1.0 km) were generated for each seismic station via ray shooting utilizing velocity models from a seismic refraction (airgun) survey recorded by the MAX-OBS network [*West et al.*, 2001]. Theoretical *S* travel times were calculated by applying a uniform *Vp*/*Vs* ratio to the *P* wave grids. Weighted-residuals were computed by comparing computed (theoretical) *P*, *S*, and *PwP* travel times with arrivals observed in the data records, with the weights being the inverse of the pick uncertainty. The grid point with the minimum weighted-residual was identified, and a fine-scale travel time grid (dx = dy = 50 m, dz = 100 m) centered on this point was constructed via interpolation. The final hypocentral estimate was determined by finding the minimum weighted-residual on the fine-scale grid.

[12] Weighted-residuals were computed employing both L1 (mean absolute deviation) and L2 (least squares) norms. Hypocentral coordinates for L1 and L2 norms are in close agreement, indicating that outliers are not exerting undue influence on the hypocenter estimates, and thus weighted root-mean square (rms) residuals (L2) were used in all subsequent error analyses. The grid-search was repeated using different *Vp*/*Vs* ratios until an empirical "best-fit" value of 1.9 was established based on minimum weighted rms residuals. This value is consistent with shallow sources and propagation through a pervasively fractured medium.

[13] Hypocenter estimates were obtained using both 1-D (average) and 3-D velocity models from the refraction data [*West et al.*, 2001]. Differences between hypocenter estimates obtained using 1-D and 3-D velocity models were generally less than a few hundred meters, even though the 3-D models contain significant lateral heterogeneities and low-velocity zones. This can be attributed to the fact that the microearthquakes originate in the shallow crust, far enough above the melt bodies such that low-velocity zones do not significantly impact body wave travel times at moderate slant ranges. As a result we employed 1-D velocity models in all subsequent analyses as they are computationally efficient and tend to stabilize higher order parameter estimates such as confidence intervals and focal mechanisms.

[14] Confidence intervals for each hypocenter were estimated from the weighted RMS residual grids described above. A three-dimensional error surface was determined for each event by identifying the spatial extent of RMS residuals less than or equal to a critical value corresponding to a specified confidence interval [*Sohn et al.*, 1998b; *Wilcock and Toomey*, 1991]. In this study the error surfaces are generally ellipsoids, because most of the hypocenters are within, or just outside, the array aperture. Error bars along the three coordinate axes were determined by projection of the error surfaces onto the coordinate planes.

[15] One hundred and forty (140) local microearthquakes were detected by four or more instruments during the deployment, and reliable hypocentral estimates could be obtained for 124 of these, with the remainder being too far removed from the networks to accurately resolve source position. Seismicity rates (of events with reliable hypocenters) during the monitoring period are shown in Figure 6, and epicenter estimates in four time windows during the

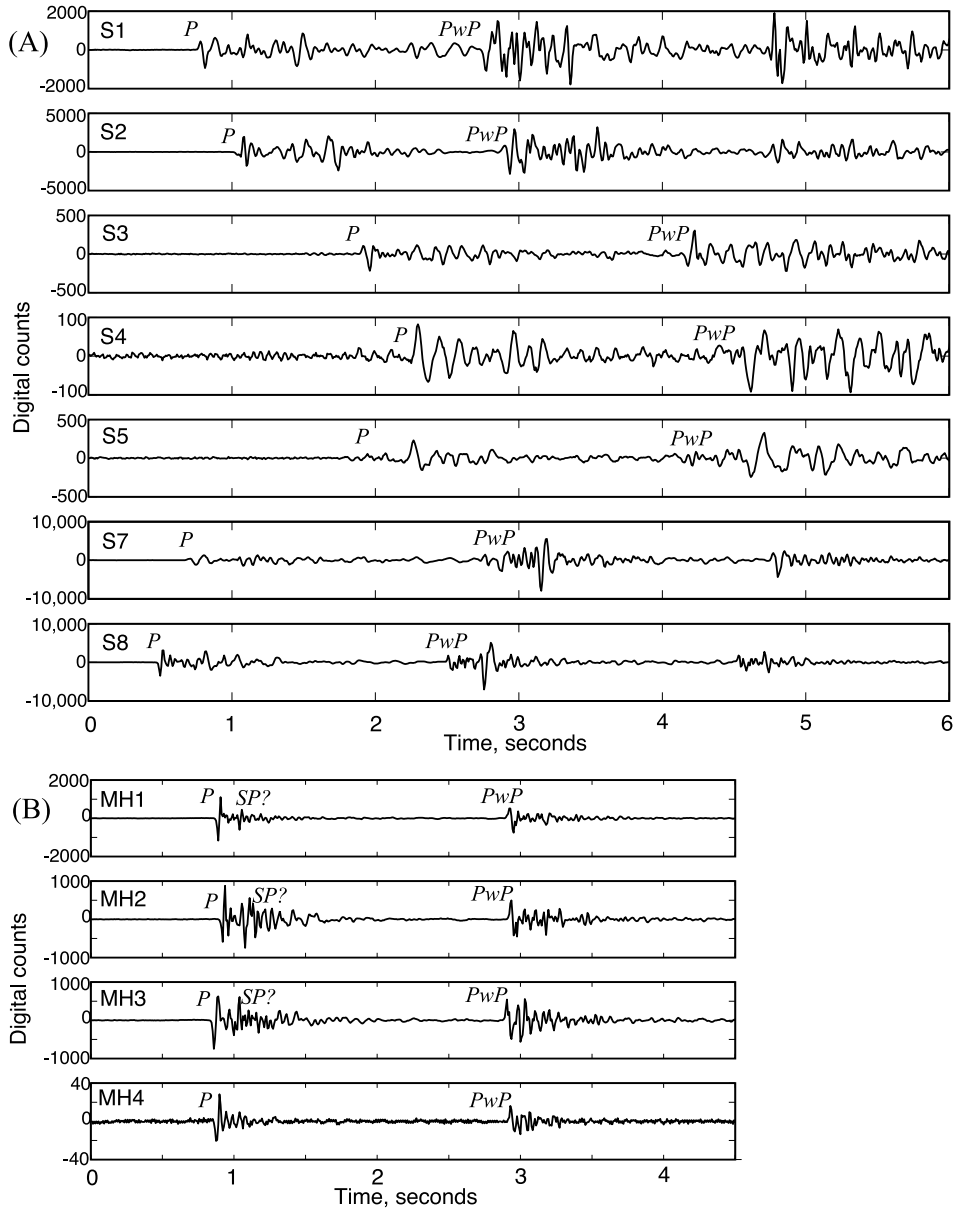

Figure 4. Example seismic records and phases from the (a) SAX and (b) MAX hydrophone deployments.

experiment are shown in Figure 7. Event hypocenters from Figure 7 are projected onto depth cross-sections in Figure 8. Hypocenters from each of the three networks were treated independently for the purpose of uncertainty analysis, and error statistics are shown in Table 1. In general, hypocentral uncertainties, and depth uncertainties in particular, are smallest for events located within the aperture of the detecting network, and somewhat larger (∼2–3x) for events located outside the network. All of the events within or near the caldera have well-constrained hypocentral coordinates with uncertainties less than or equal to the mean and median values reported in Table 1.

[16] Seismicity rates are highest at the beginning of the deployment and decay to low but steady levels within ∼60 days after the eruption (Figure 6). Initial high rates of activity are focused in the southeast corner of the caldera (Figure 7a), in the region where fresh lava flows and hydrothermal venting from the 1998 eruption were observed [*Embley et al.*, 1999]. A general trend toward quiescence is interrupted by a cluster of seismic activity on the southeast shoulder of the volcanic edifice (Figure 7b) lasting from about 100 to 150 days after the eruption. These events are located in the shallow crust immediately above a melt body (Figure 8b) that has been imaged with seismic refraction [*West*, 2001] and reflection [*Carbotte et al.*, 2002] surveys, but which has no apparent surficial expression (e.g., caldera). Seismicity rates on the volcano decrease after the cluster on the southeast shoulder and remain low until the end of the monitoring period. From 6 to 12 months after the eruption, there is still a distinct focusing of activity in the southeast corner of the caldera (Figure 7c), but from 13 to 15 months after the eruption the microearthquakes are nearly evenly distributed around the perimeter of the caldera (Figure 7d).

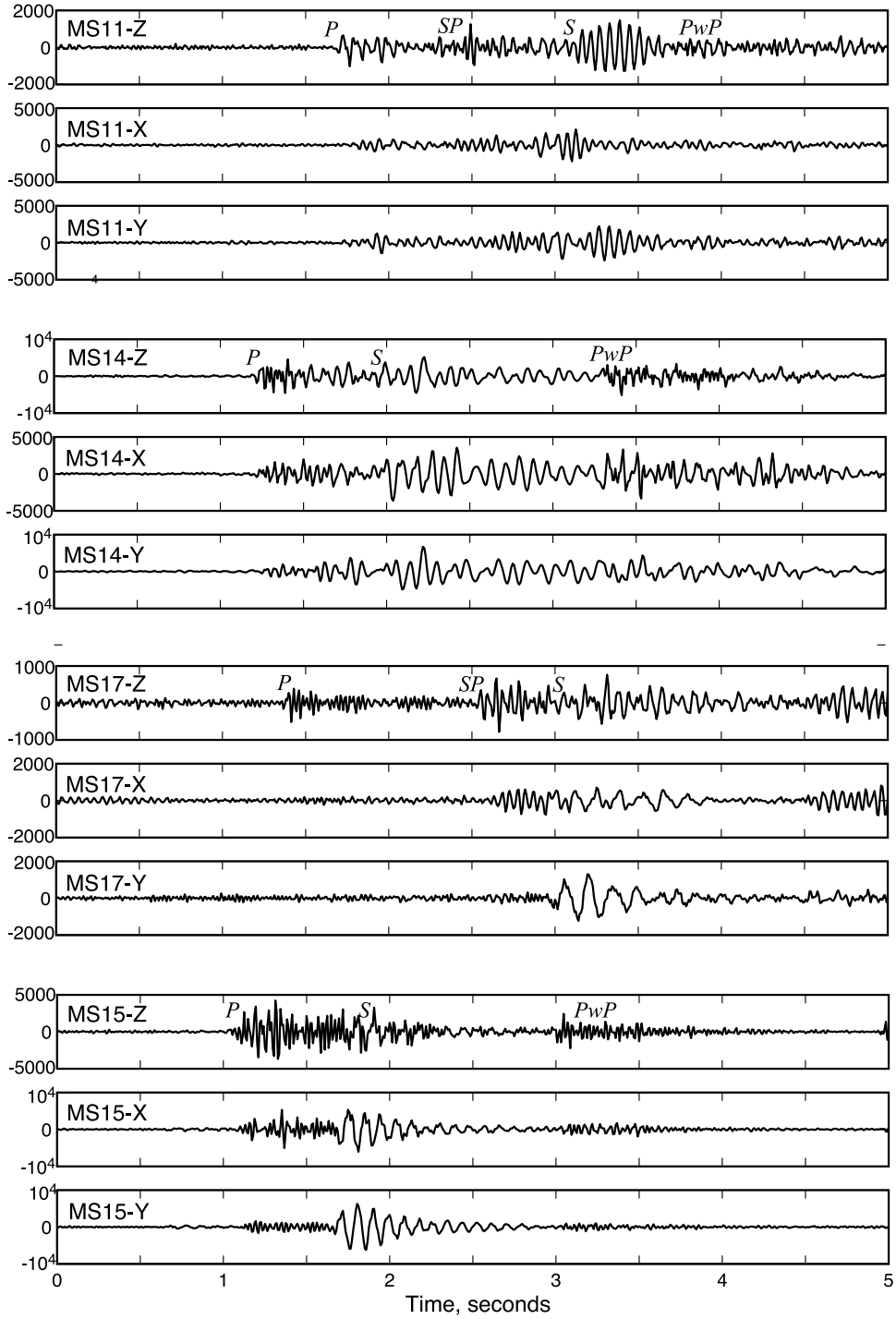

Figure 5. Example seismic records from the MAX-OBS network. One event as observed on 3-component geophone channels for 4 different stations (e.g., MS14-X is the horizontal-x channel from station 14).

[17] In general, the seismicity rates we observed after the eruption are relatively low, and are significantly lower than those observed within the caldera by a local OBH network in 1994 [*Tolstoy et al.*, 2002]. A marked decrease in hydroacoustically detected seismic activity at Axial volcano is also observed immediately after the 1998 eruption [*Dziak and Fox*, 1999b], and thus it appears that the eruption had the net effect of reducing differential stress levels in the shallow crust. This is consistent with the idea that magmatic intrusions into volcanic rift zones reduce differential tensile stresses and bring the crust back toward hydrostatic equilibrium [e.g., *Rubin*, 1992].

[18] The space-time seismicity patterns we observed are necessarily influenced by differences in the geometry of the three networks that were deployed. For example, microearthquakes along the south rift zone from 45°48–52′N could

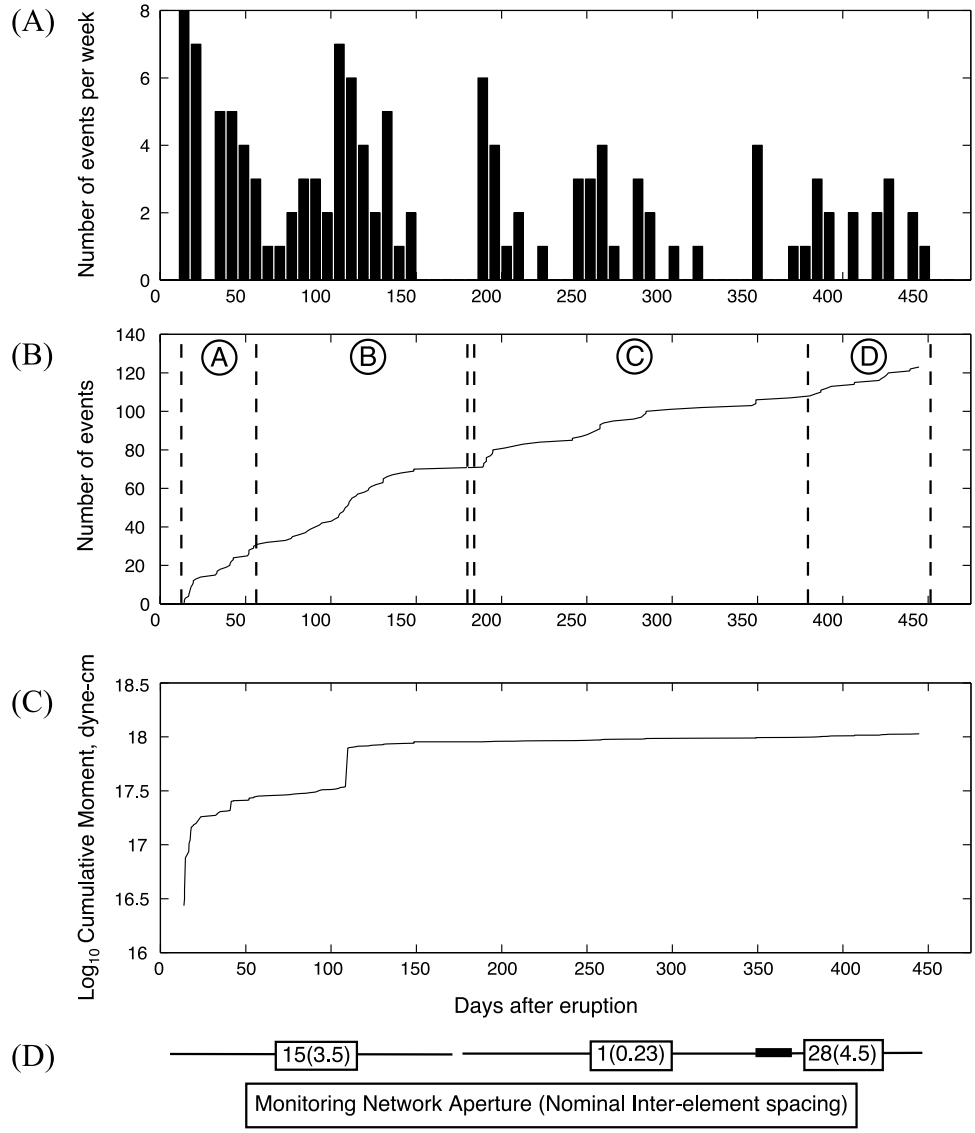

Figure 6. Seismicity rates after the eruption. (a) Histogram with weekly bins. (b) "Rate-state" cumulative number of events vs. time. Time windows corresponding to epicenter maps in Figure 10 are shown by vertical dashed lines. (c) Cumulative seismic moment. (d) Monitoring network characteristics (aperture(spacing), km). Aperture is network spread along maximum dimension. Spacing is mean value of inter-element offsets.

be located with the SAX-OBH and MAX-OBS networks, but probably not with the MAX-OBH network. However, all of the networks were able to detect and locate events within the central caldera region, and thus the systematic change from focused activity near the eruption site on the southeast corner of the caldera to distributed activity around the rim of the caldera, and the overall decrease in seismicity rates over time, are robust observations.

3.2. Earthquake Moments and Focal Mechanisms

[19] Seismic moments for each event were estimated based on long-period spectral levels of direct body phases observed on vertical geophone and hydrophone channels [*Lee and Stewart*, 1981]. Displacement spectra were estimated using multitaper techniques (time-bandwidth product of 4) [e.g., *Percival and Walden*, 1993] on 3-s data windows starting 0.3 s before the first *P* wave arrival. Displacement spectra for hydrophone data were estimated by assuming near-vertical propagation in the water and accounting for the impedance contrast at the water-rock interface. All of the events in this analysis represent small microearthquakes originating within the shallow crust. Seismic moments range from $1.3 \times 10^{14} \leq M_o \leq 4.4 \times 10^{17}$ dyne-cm, with corresponding moment magnitudes [*Kanamori*, 1977] of $-1.3 \leq M_w \leq 0.7$. Most of the total seismic moment observed during this study is released immediately after the eruption and then during the cluster on the southeast shoulder (Figure 6c). The median depth of activity is ~1 km below the seafloor, within the intrusive layer (seismic 2B).

[20] First motion polarities and focal sphere projections were used to constrain (double-couple) focal mechanisms when possible. Many events did not have unambiguous first

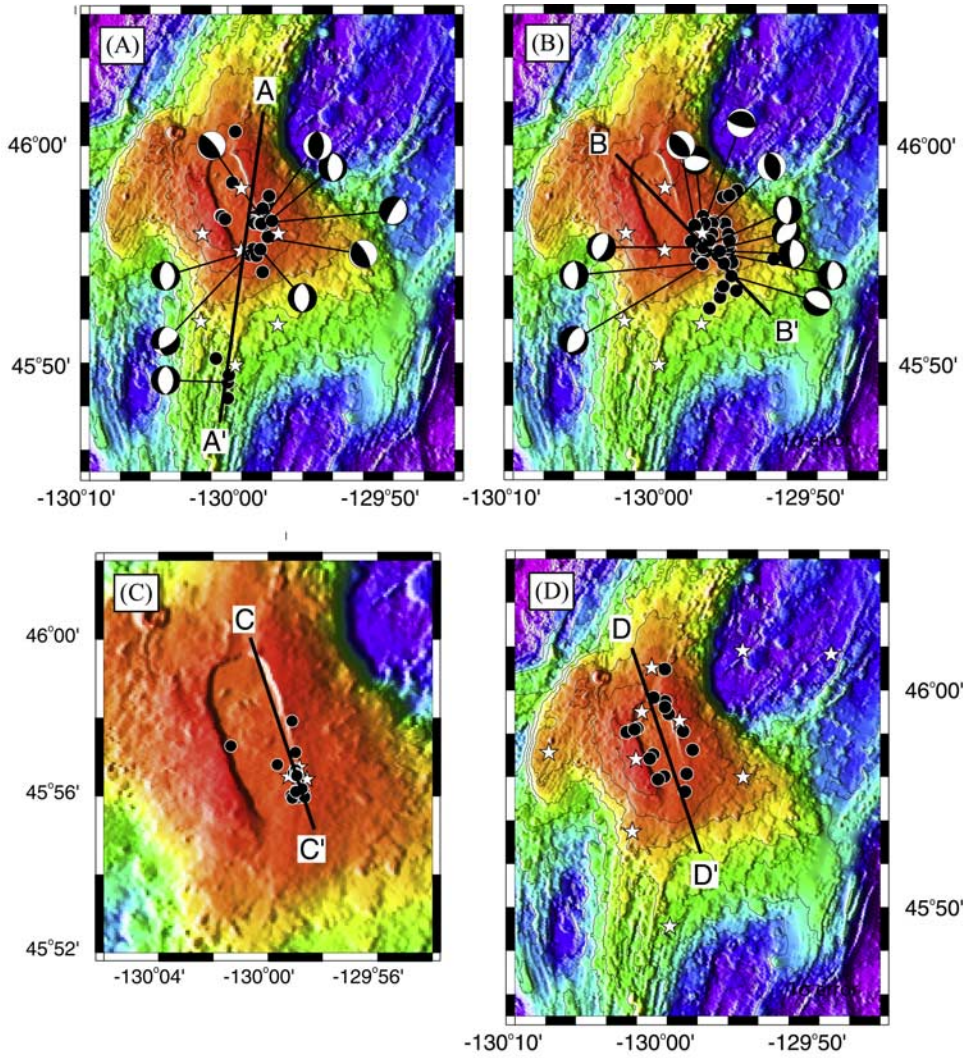

Figure 7. Epicenters during different time periods after the eruption: (a) 14–59 days post-eruption, (b) 60–180 days post-eruption, (c) 187–381 days post-eruption, and (d) 382–455 days post-eruption. Network stations shown with white stars. Focal-plane estimates are shown where possible. Hypocenter depth projections along cross-sections (i.e., AA′, BB′, etc.) are shown in Figure 8.

motion polarities on sufficient numbers of stations to allow for well-constrained focal plane solutions, but estimates could be obtained for a subset of the largest events recorded by the SAX-OBH network (Figures 7a and 7b). In most (~80%) cases, downward first motions were detected in the center of the focal sphere projection, which requires some sort of normal faulting mechanism. Interestingly, about 20% of the events with focal plane estimates have upward first motions in the center of the focal sphere, and thus apparently require a reverse faulting mechanism. On the whole, the microearthquakes observed immediately following the eruption by the SAX-OBH network are consistent with predominantly vertical slip on steep faults, similar to the focal mechanisms reported for large (teleseismic) caldera collapse events during the eruption [*Dziak and Fox*, 1999a].

[21] The assumption of double-couple source mechanisms is not always warranted in volcanic/geothermal areas [e.g., *Miller et al.*, 1998]. We will show in the discussion that volume changes associated with thermal contraction should be expected for microearthquakes within deep-sea hydrothermal systems, but the focal mechanisms shown in Plate 1a-b assume double-couple mechanisms.

4. Discussion

4.1. Microearthquake Patterns

[22] There is an obvious correlation between epicenters immediately following the eruption and the inferred location of intruded magmas. The correlation is strongest in the southeast corner of the caldera where fresh lava flows from the eruption were mapped (Figure 3), suggesting that the microearthquakes are correlated with regions where the dike approached or reached the surface. From a purely mechanical perspective, intruded magma bodies (i.e., dikes) generate compressional stress perturbations on the walls of the adjacent country rock, and tensile stress perturbations at the dike tips [e.g., *Rubin*, 1992]. Horizontal stresses in volcanic rift zones are predominantly tensile, such that lateral compression from intruded magmas perturbs the stress field back toward hydrostatic equilibrium

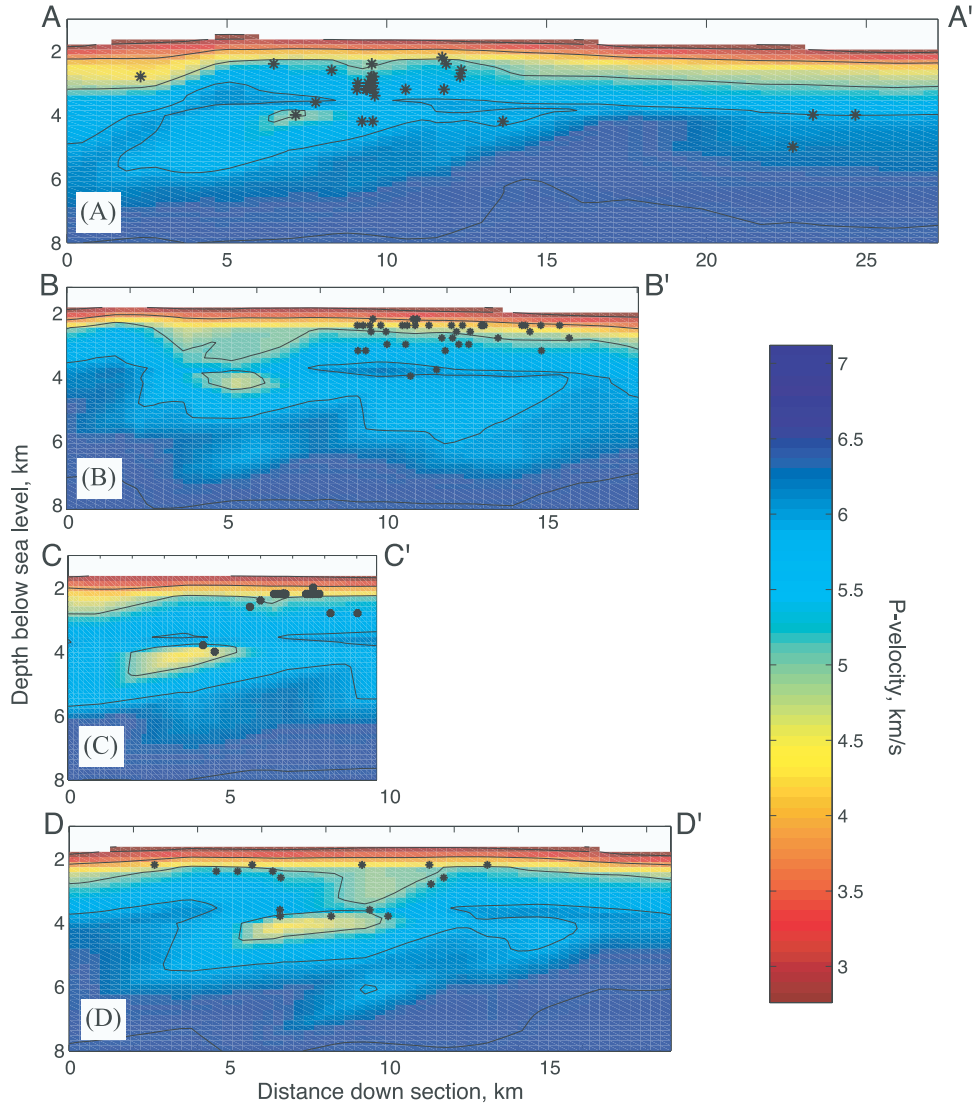

Figure 8. Hypocenter projections onto sections from Figure 7 superimposed on P wave velocity model from *West et al.* [2001]. Time windows are as per Figure 7. (a) AA′ section from 14–59 days post-eruption. (b) BB′ section from 60–180 days post-eruption. (c) CC′ section from 187–381 days post-eruption (c) DD′ section from 382–455 days post-eruption.

rather than toward tensile failure. Thus, mechanical stresses from dike intrusions are expected to cause failure and generate seismicity near dike tips [*Rubin and Gillard*, 1998], and this explains, for example, why seismic swarms migrate downrift with the dike leading edge during a rift zone intrusion [e.g., *Einarsson and Brandsdottir*, 1980]. The microearthquakes we observe in the southeast corner of the caldera immediately after the eruption are distributed along the 1998 lava flows, and thus are not easy to interpret in the context of mechanical stress perturbations at dike (top or edge) margins.

[23] Cooling of intruded magmas generates tensile stresses from thermal contraction. Definitive observations of microearthquakes generated by magma cooling are scarce

Table 1. Error Statistics for Hypocenter Estimates[a]

Error Analysis Statistics	SAX-OBH Network	MAX-OBH Network	MAX-OBS Network
σ, posterior standard deviation, s	0.096	0.03	0.135
N, degrees of freedom	363	143	82
E_x, km[b]	mean = 1.6 median = 1.25	mean = 0.72 median = 0.25	mean = 1.1 median = 1.0
E_y, km[b]	mean = 1.2 median = 0.63	mean = 1.0 median = 0.25	mean = 1.0 median = 0.88
E_z, km[b]	mean = 1.44 median = 0.75	mean = 0.67 median = 0.5	mean = 1.41 median = 1.25

[a] E_x, E_y, and E_z are the 1σ errors in the *x*-, *y*-, and *z*-directions for each event. The *y axis* is oriented with the ridge strike (26° true), the *x* axis is oriented perpendicular to the ridge strike (116° true), and the *z* axis is oriented vertically. Hypocenter error parameters were estimated following *Wilcock and Toomey* [1991] and *Sohn et al.* [1998b].

[b] All error bars are presented at the 66% (1σ) level.

in the literature [e.g., *Chouet*, 1979], but this may be largely attributed to the fact that seismic networks are rarely deployed in small enough configurations to observe the very small events triggered by this process. We examine quantitative aspects of thermal cracking below (section 4.2), but we note here that the space-time patterns of observed microearthquake activity beneath the 1998 flows are consistent with this mechanism. Seismicity rates near the 1998 flows are highest immediately following the eruption when cooling rates are also highest. Elevated seismicity rates persist until ~60 days after the eruption, and this timescale is consistent with essentially complete cooling of a ~2-m-wide dike [*Cherkaoui et al.*, 1997].

[24] The cluster of microearthquakes on the southeast shoulder of the volcano from 100 to 150 days after the eruption is directly above a recently discovered mid-crustal low-velocity zone/melt body [*West*, 2001; *Carbotte et al.*, 2002] (Figure 8b). The vertical fault plane solutions obtained for many of these events are consistent with some sort of subsidence event, and it seems likely that the microearthquakes were triggered by thermal or mechanical (pressure) changes within the underlying melt reservoir. Interestingly, a pulse of hydrothermal fluids measured on moorings in the caldera region was attributed to a source on the southeast shoulder during this same time [*Lavelle et al.*, 2001], suggesting that the microearthquakes were accompanied by a local hydrothermal perturbation.

[25] The events on the southeast shoulder were previously attributed to a tectonic process associated with either spreading on the JdFR or gravitational stresses on the volcano's flank [*Sohn et al.*, 1999a], but this interpretation now seems unlikely given the position of the events directly above a mid-crustal melt body. We can only speculate regarding the exact cause of these events, but a magmatic process, such as cooling and/or subsidence, seems most likely. There is no evidence that the satellite melt reservoir under the southeast shoulder has produced any volcanic eruptions, but its connectivity with the main melt reservoir is unknown. A better understanding of the relationship between the two melt reservoirs is critical to understanding the magma dynamics of Axial Volcano, and this would appear to be a fruitful area of research in the future.

[26] Events observed by the small-aperture MAX-OBH network 187–381 days after the eruption are closely correlated with the position of the 1998 lava flow in the southeast corner of the caldera (Figure 3). A 3-D perspective view of these events (Figure 9) reveals that there are two distinct clusters in the shallow crust, with each cluster corresponding to the position of a large vent field on the seafloor within the 1998 lava flow. The northern cluster, which is more tightly constrained because it is within the seismic network, is ~0.7 km beneath the Pit vent, and the southern cluster is at a similar depth beneath the Cloud vent. These events did not occur in swarms, as has been observed for instance beneath hydrothermal vent fields on the EPR [*Sohn et al.*, 1999b] and Middle Valley of the JdFR [*Golden et al.*, 2003], but rather occur at relatively steady rates throughout the observation period.

[27] These microearthquakes add to the growing body of evidence that cooling of hot rock within the hydrothermal water-rock reaction zone generates small magnitude ($M_w \sim 0$), microearthquakes that can be observed with small-aperture ocean bottom seismic networks. Under this interpretation the microearthquakes delineate the subsurface position of the water-rock reaction zone, and thus provide important constraints on the physical patterns of hydrothermal circulation. The depths of the events beneath the Pit and Cloud vent fields are well-constrained to be within 0.5–1.0 km of the seafloor, indicating that the water-rock reaction zone is about 2 km above the crustal melt reservoir. This implies a relatively thick thermal boundary layer above the magma chamber following the 1998 eruption.

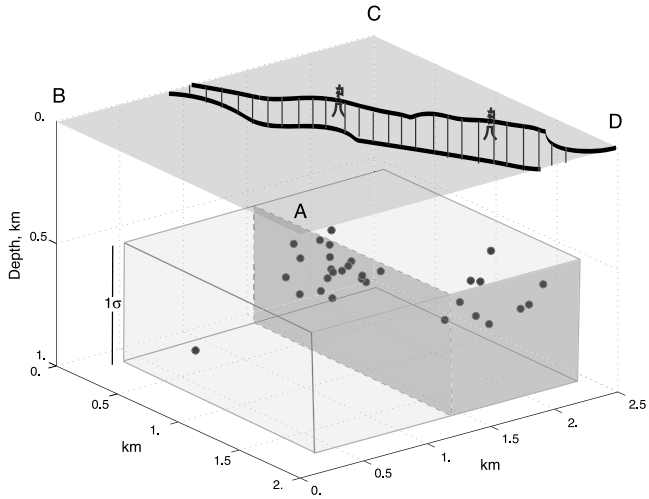

Figure 9. A 3-D perspective view of microearthquakes observed by the MAX-OBH network beneath the 1998 lava flow. Depth confidence intervals for all events are between 0.5 and 1.0 km. Surface position of hydrothermal vents and lava flows are from R. W. Embley and W. W. Chadwick (unpublished data, 2003).

[28] We attempted to apply waveform cross-correlation techniques [e.g., *Shearer*, 1997] to obtain relative locations for the microearthquakes beneath the Cloud and Pit vent fields, but we were unable to obtain coherent sets of correlated events at individual stations. Most of the data records from the MAX-OBH network contain a second impulsive phase that arrives just after the direct *P* wave (Figure 4b). The delay time of this phase moves out with slant range at approximately the *S* wave velocity of seismic layer 2B (Figure 10), but the phase arrives too early to be a direct *S* wave, and is robust in hydrophone pressure records, which argues against predominantly horizontal particle motion. These first-order considerations suggest that the phase is an *S* to *P* conversion, or perhaps a *P-P* underside reflection. In any case, it cannot be filtered from the data without losing the direct *P* wave and thus presents a serious obstacle to relative relocation techniques. Interestingly, cross-correlation coefficients are high between waveforms from individual events observed at different stations. This is a departure from the usual paradigm exploited for relative relocation methods (high correlations between multiple events observed at single stations), and requires that the source radiation pattern and propagation effects are similar for all of the stations observing a single event.

[29] Microearthquakes observed by the MAX-OBS network during the last 70 days of our observation period

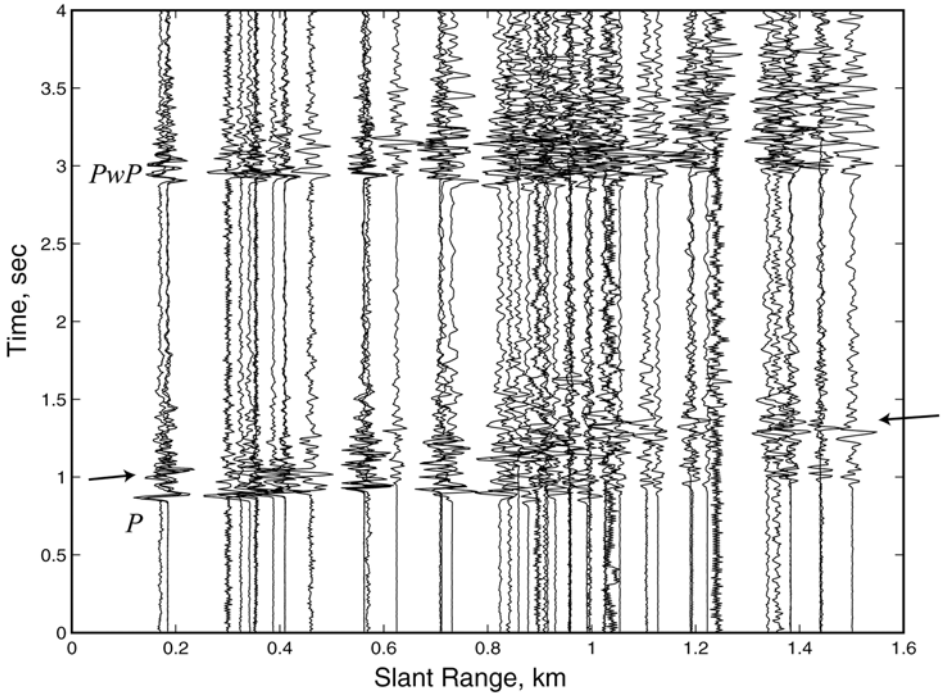

Figure 10. Pseudo-record section from the MAX-OBH network showing second phase (delineated with arrows) arriving directly after the direct P body wave.

(382–455 days post-eruption) are distributed in a ring around the caldera (Figure 7d). The aperture and instrument spacing of the MAX-OBS network were too large to detect small magnitude thermal cracking events beneath the southeast corner of the caldera (as observed by the MAX-OBH network), but the instruments were well positioned to observe faulting around the caldera. Focal mechanism estimates could not be made for any of these events, but it seems likely that they represent small amounts of slip along the nearly vertical caldera faults. The simplest explanation is that they are small normal faulting events associated with continuing, but relatively minor, caldera subsidence following the magmatic event.

[30] We did not observe any correlation between the timing of caldera events and the ocean tides. This contrasts with results reported previously by *Tolstoy et al.* [2002], who found a correlation between microearthquake activity and low ocean tides at Axial in 1994. There are two possible explanations for the lack of correlation between microearthquake triggering and ocean tides in our data. It is possible that we simply did not detect enough events to allow for a statistical establishment of weak correlation. Tests for weak correlation are only rigorous when the number of events is very large, and the low seismicity rates during our deployment may preclude a rigorous hypothesis test in this case.

[31] However, we observed seismic activity over a 15-month period, which is almost an order of magnitude longer time period than the *Tolstoy et al.* [2002] deployment (2 months). The absence of an observable link between tides and microearthquake triggering in our data set is therefore significant, and, if we accept that tides triggered earthquakes in the caldera region in 1994, it is difficult to escape the conclusion that the eruption in 1998 reduced the sensitivity of the earthquake generating process to ocean tide pressure perturbations. This is not surprising considering that the eruption dramatically reduced seismicity rates overall, which is a well-documented phenomenon in the magmatic-tectonic cycle of rift zone volcanoes [e.g., *Rubin*, 1992]. Perhaps the simplest explanation is that the magmatic event reduced differential stresses in the shallow crust and reset a predominantly tensile stress environment to near lithostatic conditions, such that the relatively small stress perturbations induced by tidal loading were no longer sufficient to trigger seismicity. It is also possible that melt removal from the magma chamber effectively stiffened the overlying crustal column, and thus reduced the compliance contrast (which describes the depression under loading) across caldera faults.

4.2. Thermal Cracking in Deep-Sea Hydrothermal Systems

[32] Small microearthquakes are ubiquitous in records from seismometers deployed near deep-sea hydrothermal systems [*Golden et al.*, 2003; *McClain et al.*, 1993; *Riedesel et al.*, 1982; *Sohn et al.*, 1999b, 1995; *Tolstoy et al.*, 2002; *Wilcock*, 2001]. Causal links between vent field microearthquakes and exit-fluid temperatures have been established [*Sohn et al.*, 1998a], and in some cases the microearthquakes appear to be triggered by thermal cracking as hydrothermal fluids cool and penetrate hot igneous rocks [*Golden et al.*, 2003; *Sohn et al.*, 1999b].

[33] The heat flux from individual high-temperature hydrothermal vents is believed to range from 0.1 to 100 MW [*Ginster et al.*, 1994], and thermal strain rates associated with these values are at least 2–3 orders of magnitude higher than tectonic strain rates [*Cowie et al.*, 1993] for volcanically active spreading centers [*Sohn et al.*, 1999b]. Here we model the stresses induced in the rock as it slowly cools at temperatures below the rigidus. We find that small temper-

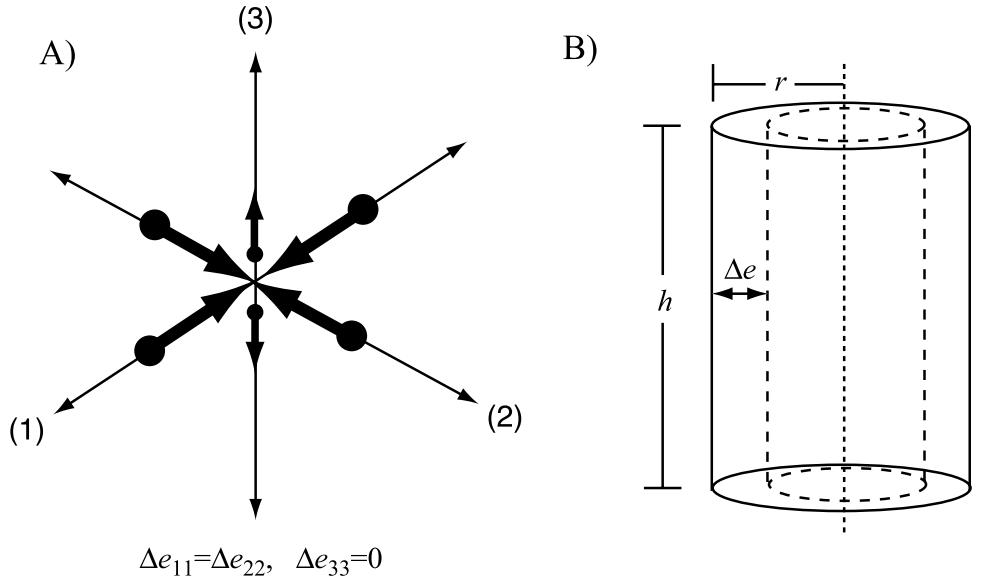

Figure 11. (a) Body force representation for thermal cracking in the water-rock reaction zone of a deep-sea hydrothermal system. Contraction is uniform in the horizontal directions, but cracks do not open vertically because of overburden. This gives rise to cylindrical source volumes as shown in Figure 11b, where the transformational strain is uniform in the horizontal plane.

ature changes produce stresses sufficient to cause failure under thermal contraction, and we use the amplitude of the microearthquakes to estimate the source volumes associated with the events we observe beneath vent fields.

[34] Thermoelastic processes are fundamental to the physics of deep-sea hydrothermal systems [e.g., *Germanovich et al.*, 2001; *Lowell*, 1990]. Thermal contraction in the water-rock reaction zone generates cracks when elastic stresses achieve some threshold value associated with mode I type failure (tensile crack opening). Thermal contraction in an isotropic medium with overburden produces horizontal strain [e.g., *Lister*, 1974], which generates strain discontinuities (Δe) in a source volume that are normal to the horizontal axes (i.e., $\Delta e_{11} = \Delta e_{22}$, $\Delta e_{33} = 0$). This dilatational source mechanism (Figure 11) is slightly different than the tensile crack models that have been proposed previously for short-period volcanic events [e.g., *Shimizu et al.*, 1987] because of our assumption of horizontal plane strain. We can use transformational strain concepts [*Eshelby*, 1957] to develop an expression (see Appendix A) for the moment tensor associated with thermal cracking in deep-sea hydrothermal reaction zone. The scalar seismic moment for this source mechanism is

$$M_0 = \frac{2}{\sqrt{3}}\Delta e V\left[2(\lambda+\mu)^2+\lambda^2\right]^{1/2}, \tag{1}$$

where λ and μ are the Lame parameters, and V is source volume. The Lame parameters for the shallow crust at Axial volcano are fairly well constrained by the combination of seismic refraction data, seafloor gravity measurements [*Hildebrand et al.*, 1990], and our microearthquake data (V_p/V_s ratio). With Lame parameters of λ = 35 GPa and μ = 12 GPa, we can express the scalar seismic moment as a function of the strain released by a cracking event,

$$M_0 = 12 \times 10^{11} V \Delta e. \tag{2}$$

Following *Lister* [1974], the equivalent uniaxial stress from thermal contraction is

$$\sigma_H = \frac{E}{\eta}\alpha\Delta T, \tag{3}$$

where E is Young's modulus, η is Poisson's ratio, α is thermal expansivity of basalt, and ΔT is the amount of cooling. The amount of cooling, and thus differential strain, associated with failure during thermal cracking depends on the yield strength of the cooling rock. Here we assume that failure will occur when horizontal differential stress equals or exceeds lithostatic (i.e., $\sigma_H \geq \bar{\rho}gz$ where, $\bar{\rho}$ is mean crustal density above the cracking event and z is event depth). This assumption could be amended with a more exhaustive treatment of rock mechanics, but we do not attempt that here.

[35] If we assert that seismic failure occurs when horizontal stresses reach lithostatic values, and again use the geophysical data acquired at Axial to constrain the elastic parameters (E = 33 GPa, η = 0.37), then using a standard value of $\alpha = 8 \times 10^{-6}$ K^{-1} we can directly relate differential stress to cooling temperature,

$$\Delta T = z\left(\frac{\bar{\rho}g\eta}{E\alpha}\right) = 3.8 \times 10^{-2} z, \tag{4}$$

where ΔT is in °K and is in meters. The amount of cooling required for failure is a function of depth since our failure criterion is set to lithostatic, but is relatively small in any case since the nominal depth of cracking in submarine volcanic systems is on the order of 10^2–10^3 m. For the MAX-OBH events beneath the Cloud and Pit vent fields, with event depths of ~0.7 km, equation (4) yields a value of $\Delta T \sim 27$°C. Thus the thermal contraction generated by cooling a layer of rock at shallow depths by 27°C is sufficient to cause failure and open tensile cracks.

[36] The maximum differential strain associated with thermal cracking can now be directly estimated. For horizontal plane strain,

$$\Delta e = 2\alpha\Delta T, \tag{5}$$

and thus we obtain the general relationship for the Axial volcano caldera region,

$$\Delta e = 6.1 \times 10^{-7} z, \tag{6}$$

with in meters as before. Using source depths of 0.7 km, we obtain $\Delta e = 4.3 \times 10^{-4}$ for the strain associated with the events we observe beneath the Cloud and Pit vent fields.

[37] With constraints on the differential strain of a cracking event, we can use equation (1) to directly relate the seismic moment of the observed microearthquakes to source volumes. At Axial we find that source volumes ranging from $0.3 \leq V \leq 19$ m^3 experience corresponding volume changes of $1.3 \times 10^{-4} \leq \Delta V \leq 8.2 \times 10^{-3}$ m^3, with mean values of $V = 4.8$ m^3 and $\Delta V = 2.0 \times 10^{-3}$ m^3. The microearthquakes beneath the Pit and Cloud vent fields are thus consistent with cracking from volume changes of $\sim 2 \times 10^{-3}$ m^3 resulting from temperature changes of $\sim$27°C in average source volumes of about 5 m^3.

[38] We can estimate the heat flux associated with the microearthquakes we observe beneath the Cloud and Pit vent fields by assuming that each event represents 27°C cooling of a source volume related to scalar seismic moment by equation (1). Using these relationships, we obtain a total heat release of 3.8×10^9 J and 7.4×10^9 J associated with seismicity beneath the Cloud and Pit vents, respectively. During our 194-day observation period (MAX-OBH network), this yields heat flow values of 227 W and 441 W for Cloud and Pit, respectively. The heat flow associated directly with thermal cracking (200–400 W) is thus only a tiny fraction ($<1 \times 10^{-3}$) of the heat flow estimates for black smokers (0.1–100 MW) [*Ginster et al.*, 1994].This indicates that most of the stress from thermal contraction must be released by transient creep at temperatures above or near the rigidus, or by small undetectable events.

5. Summary

[39] 1. We obtained hypocentral estimates for 140 local microearthquakes detected by ocean bottom seismic networks during 15 months of observation following the January 1998 eruption of Axial volcano. The post-eruption seismicity rates are several orders of magnitude less than those observed prior to the magmatic event.

[40] 2. Apart from a burst of activity on the southeast shoulder of the volcano, seismicity rates steadily decline following the 1998 eruption, and seismic patterns evolve from focused activity beneath the eruption area in the southeast corner of the caldera to distributed activity around the caldera faults. The low seismicity rates observed following the eruption demonstrate that nearly all of the earthquakes generated by a magmatic event are triggered during magma movement, and that local seismic monitoring networks must be in place before a magmatic event if these earthquakes are to be used to place constraints on the subsurface position of the propagating magma bodies.

[41] 3. The anomalous cluster of events on the southeast shoulder of the volcano overly a recently imaged satellite melt reservoir.

[42] 4. Hypocenters for all well-constrained events lie within the uppermost 2 km of crust.

[43] 5. A small-aperture network deployed within the eruption area on the southeast corner of the caldera detected two clusters of microearthquakes beneath the vent fields in this area. Assuming that these earthquakes are triggered by thermal cracking in the hydrothermal water-rock reaction zone, they are consistent with average volume changes of 2×10^{-3} m^3 associated with $\sim$27°C cooling of $\sim$5 m^3 source volumes. The strain rates expected from thermal contraction are easily sufficient to explain the observed seismicity.

[44] 6. The timing of the observed seismic activity is not correlated with ocean tides.

Appendix A: Derivation of Seismic Moment Tensor for Thermal Cracking in Deep-Sea Hydrothermal Systems

[45] The seismic moment density tensor for a volume source can be defined as

$$m_{pq} = [\Delta e_i] v_j c_{ijpq}, \tag{A1}$$

where v_j are the outward normals and c_{ijpq} are the elastic constants [*Aki and Richards*, 1980]. Under the assumption of horizontal plane strain, which is appropriate for thermal contraction in the presence of overburden, we have $\Delta e_{11} = \Delta e_{22}$, $\Delta e_{33} = 0$ (see Figure 11). If we assume an isotropic medium (i.e., $c_{ijpq} = \lambda\delta_{ij}\delta_{pq} + \mu\,(\delta_{ip}\delta_{jq} + \delta_{iq}\delta_{jp})$ [*Jeffreys and Jeffreys*, 1972]), then we can calculate the seismic moment density tensor,

$$\mathbf{m} = -\begin{bmatrix} 2\Delta e(\lambda+\mu) & 0 & 0 \\ 0 & 2\Delta e(\lambda+\mu) & 0 \\ 0 & 0 & 2\Delta e\lambda \end{bmatrix}, \tag{A2}$$

where λ and μ are the Lame parameters. The moment tensor is then found by integrating over the source volume,

$$\mathbf{M} = -V\begin{bmatrix} 2\Delta e(\lambda+\mu) & 0 & 0 \\ 0 & 2\Delta e(\lambda+\mu) & 0 \\ 0 & 0 & 2\Delta e\lambda \end{bmatrix}. \tag{A3}$$

Following *Dahlen and Tromp* [1998], the scalar moment, M_0, of an arbitrary moment-tensor, $\mathbf{M}$, is defined as

$$M_0 = \frac{1}{\sqrt{3}}(\mathbf{M} : \mathbf{M})^{1/2}. \tag{A4}$$

where the $\sqrt{3}$ normalization is used to account for the dilatational source mechanism. Now we obtain the general expression for the scalar moment of dilatational thermal cracking events in deep-sea hydrothermal systems,

$$M_0 = \frac{2}{\sqrt{3}}\Delta e V\left[2(\lambda+\mu)^2 + \lambda^2\right]^{1/2}(\text{mks}). \tag{A5}$$

[46] **Acknowledgments.** Our field program, encompassing three research legs over a 1.5-year period, owes its success to a host of scientists,

engineers, technicians, and marine crew far too numerous to list here. We are particularly grateful to Wayne Crawford, Jacques Lemire, Tom Deaton, Charles Golden, Valerie Ballu, and Mike West for assistance preparing and deploying the seafloor seismic networks, and to Bob Embley, Bill Chadwick, Bob Dziak, and Chris Fox for coordinating the 1998 rapid response effort and sharing data. Raytracing was accomplished using algorithms provided by Bill Menke, and seismic velocity models provided by West, Menke, and Maya Tolstoy. Many of the figures were prepared using the GMT software developed by Paul Wessel and Walter Smith. The manuscript benefited from thoughtful reviews by Chadwick and two anonymous reviewers. Sohn, Webb, and the field program were supported by NSF grant OCE 97-11700. Barclay was supported in part by the Woods Hole Oceanographic Institution.

References

Aki, K., and P. G. Richards (1980), *Quantitative Seismology, Theory and Methods*, W. H. Freeman, New York.

Carbotte, S. M., et al. (2002), A multi-channel seismic investigation of ridge crest and ridge flank structure along the Juan de Fuca Ridge, *Eos. Trans. AGU*, *83*(47), Fall Meet. Suppl., Abstract T72C-07.

Chadwick, W. W., Jr., R. W. Embley, H. B. Milburn, C. Meinig, and M. F. Stapp (1999), Evidence for deformation associated with the 1998 eruption of Axial Volcano, Juan de Fuca Ridge, from acoustic extensometer measurements, *Geophys. Res. Lett.*, *26*, 3441–3444.

Cherkaoui, A. S. M., W. S. D. Wilcock, and E. T. Baker (1997), Thermal fluxes associated with the 1993 diking event on the CoAxial Segment, Juan de Fuca Ridge: A model for the convective cooling of a dike, *J. Geophys. Res.*, *102*, 24,887–24,902.

Chouet, B. (1979), Sources of seismic events in the cooling lava lake of Kilauea Iki, Hawaii, *J. Geophys. Res.*, *84*, 2315–2330.

Cowie, P. A., C. H. Scholz, M. Edwards, and A. Malinverno (1993), Fault strain and seismic coupling on mid-ocean ridges, *J. Geophys. Res.*, *98*, 17,911–17,920.

Dahlen, F. A., and J. Tromp (1998), *Theoretical Global Seismology*, 1025 pp., Princeton Univ. Press, Princeton, N. J.

Dalrymple, G. B., D. A. Clague, and T. L. Vallier (1987), 40Ar/39Ar age, petrology, and tectonic significance of some seamounts in the Gulf of Alaska, in *Seamounts, Islands, and Atolls*, edited by B. H. Keating et al., pp. 297–315, AGU, Washington, D. C.

Desonie, D. L., and R. A. Duncan (1990), The Cobb-Eickelberg Seamount Chain: Hotspot volcanism with mid-ocean ridge basalt affinity, *J. Geophys. Res.*, *95*, 12,697–12,712.

Dziak, R. P., and C. G. Fox (1999a), The January 1998 earthquake swarm at Axial Volcano, Juan de Fuca Ridge: Hydroacoustic evidence of seafloor volcanic activity, *Geophys. Res. Lett.*, *26*, 3429–3432.

Dziak, R. P., and C. G. Fox (1999b), Long-term seismicity and ground deformation at Axial Volcano, Juan de Fuca Ridge, *Geophys. Res. Lett.*, *26*, 3641–3644.

Einarsson, P., and B. Brandsdottir (1980), Seismological evidence for lateral magma intrusion during the July 1978 deflation of the Krafla Volcano in NE Iceland, *J. Geophys.*, *47*, 160–165.

Embley, R. W., W. W. Chadwick Jr., D. A. Clague, and D. Stakes (1999), 1998 eruption of Axial Volcano: Multibeam anomalies and sea-floor observations, *Geophys. Res. Lett.*, *26*, 3425–3428.

Eshelby, J. D. (1957), The determination of the elastic field of an ellipsoidal inclusion, and related problems, *Proc. R. Soc. London, Ser. A*, *241*, 376–396.

Fox, C. G. (1999), In situ ground deformation measurements from the summit of Axial Volcano during the 1998 volcanic episode, *Geophys. Res. Lett.*, *26*, 3437–3440.

Fox, C. G., R. P. Dziak, H. Masumoto, and A. E. Schreiner (1994), Potential for monitoring low-level seismicity on the Juan de Fuca Ridge using military hydrophone arrays, *Marine Tech. Soc. J.*, *27*(4), 22–30.

Fox, C. G., W. W. Chadwick Jr., and R. W. Embley (2001), Direct observation of a submarine volcanic eruption from a sea-floor instrument caught in a lava flow, *Nature*, *412*, 727–729.

Germanovich, L. N., R. P. Lowell, and D. K. Astakhov (2001), Temperature-dependent permeability and bifurcations in hydrothermal flow, *J. Geophys. Res.*, *106*, 473–496.

Ginster, U., M. J. Mottl, and R. P. Von Herzen (1994), Heat flux from black smokers on the Endeavour and Cleft segments, Juan de Fuca Ridge, *J. Geophys. Res.*, *99*, 4937–4950.

Golden, C. E., S. C. Webb, and R. A. Sohn (2003), Hydrothermal microearthquake swarms beneath active vents at Middle Valley, Northern Juan de Fuca Ridge, *J. Geophys. Res.*, *108*(B1), 2027, doi:10.1029/2001JB000226.

Hildebrand, J. A., J. M. Stevenson, P. T. C. Hammer, M. A. Zumberge, R. L. Parker, C. G. Fox, and P. J. Meis (1990), A seafloor and sea surface gravity survey of Axial Volcano, *J. Geophys. Res.*, *95*, 12,753–12,764.

Jeffreys, H., and B. S. Jeffreys (1972), *Methods of Mathematical Physics*, Cambridge Univ. Press, New York.

Kanamori, H. (1977), The energy release in great earthquakes, *J. Geophys. Res.*, *82*, 2981–2987.

Lavelle, J. W., M. A. Wetzler, E. T. Baker, and R. W. Embley (2001), Prospecting for hydrothermal vents using moored current and temperature data: Axial Volcano on the Juan de Fuca Ridge, northeast Pacific, *J. Phys. Oceanogr.*, *31*(3), 827–838.

Lee, W. H. K., and S. W. Stewart (1981), *Principles and Applications of Microearthquake Networks*, Academic, San Diego, Calif.

Lister, C. R. B. (1974), On the penetration of water into hot rock, *Geophys. J. R. Astron. Soc.*, *39*, 465–509.

Lowell, R. P. (1990), Thermoelasticity and the formation of black smokers, *Geophys. Res. Lett.*, *17*, 709–712.

McClain, J. S., M. L. Begnaud, M. A. Wright, J. Fondrk, and G. K. Von Damm (1993), Seismicity and tremor in a submarine hydrothermal field: The Northern Juan de Fuca Ridge, *Geophys. Res. Lett.*, *20*, 1883–1886.

Menke, W., M. West, and M. Tolstoy (2002), Shallow-crustal magma chamber beneath the axial high of the CoAxial Segment of Juan de Fuca Ridge at the source site of the 1993 eruption, *Geology*, *30*, 359–362.

Miller, A. D., G. R. Foulger, and B. R. Julian (1998), Non-double-couple earthquakes: 2. Observations, *Rev. Geophys.*, *36*, 551–568.

Percival, D. B., and A. T. Walden (1993), *Spectral Analysis for Physical Applications: Multitaper and Conventional Univariate Techniques*, 583 pp., Cambridge Univ. Press, New York.

Riedesel, M., J. A. Orcutt, K. C. MacDonald, and J. S. McClain (1982), Microearthquakes in the black smoker hydrothermal field, East Pacific Rise at 21°N, *J. Geophys. Res.*, *87*, 10,613–10,623.

Rubin, A. M. (1992), Dike-induced faulting and graben subsidence in volcanic rift zones, *J. Geophys. Res.*, *97*, 1839–1858.

Rubin, A. M., and D. Gillard (1998), Dike-induced earthquakes: Theoretical considerations, *J. Geophys. Res.*, *103*, 10,017–10,030.

Shearer, P. M. (1997), Improving local earthquake locations using the L1 norm and waveform cross correlation: Application to the Whittier Narrows, California, aftershock sequence, *J. Geophys. Res.*, *102*, 8269–8283.

Shimizu, H., S. Ueki, and J. Koyama (1987), A tensile-shear crack model for the mechanism of volcanic earthquakes, *Tectonophysics*, *144*, 287–300.

Sohn, R. A., J. A. Hildebrand, S. C. Webb, and C. G. Fox (1995), Hydrothermal microseismicity at the megaplume site on the Southern Juan de Fuca Ridge, *Bull. Seismol. Soc. Am.*, *85*(3), 775–786.

Sohn, R. A., D. Fornari, K. L. Von Damm, J. A. Hildebrand, and S. C. Webb (1998a), Seismic and hydrothermal evidence for a cracking event on the East Pacific Rise crest at 9°50′N, *Nature*, *396*, 159–161.

Sohn, R. A., J. A. Hildebrand, and S. C. Webb (1998b), Post-rifting seismicity and a model for the 1993 diking event on the CoAxial segment, Juan de Fuca Ridge, *J. Geophys. Res.*, *103*, 9867–9877.

Sohn, R. A., W. C. Crawford, and S. C. Webb (1999a), Local seismicity following the 1998 eruption of Axial Volcano, *Geophys. Res. Lett.*, *26*, 3433–3436.

Sohn, R. A., J. A. Hildebrand, and S. C. Webb (1999b), A microearthquake survey of the high-temperature vent fields on the volcanically active East Pacific Rise, *J. Geophys. Res.*, *104*, 25,367–25,378.

Tolstoy, M., F. L. Vernon, J. A. Orcutt, and F. K. Wyatt (2002), Breathing of the seafloor: Tidal correlations of seismicity at Axial Volcano, *Geology*, *30*, 503–506.

West, M. E. (2001), The deep structure of Axial Volcano, Ph.D. dissertation, 129 pp., Columbia Univ., New York.

West, M., W. Menke, M. Tolstoy, S. C. Webb, and R. A. Sohn (2001), Magma storage beneath Axial volcano on the Juan de Fuca mid-ocean ridge, *Nature*, *413*, 833–836.

Wilcock, W. S. D. (2001), Tidal triggering of microearthquakes on the Juan de Fuca Ridge, *Geophys. Res. Lett.*, *28*, 3999–4002.

Wilcock, W. S. D., and D. R. Toomey (1991), Estimating hypocentral uncertainties for marine microearthquake surveys: A comparison of the generalized inverse and grid search methods, *Mar. Geophys. Res.*, *13*(2), 161–171.

A. H. Barclay, University of Washington, School of Oceanography, Seattle, WA 98195, USA. (andrew@ocean.washington.edu)

R. A. Sohn, Woods Hole Oceanographic Institution, Woods Hole, MA 02543, USA. (rsohn@whoi.edu)

S. C. Webb, Lamont Doherty Earth Observatory, Palisades, NY 10964, USA. (scw@ldeo.columbia.edu)